


Localized dimers drive strong anharmonicity and low lattice thermal conductivity in ZnSe₂Tiantian Jia,^{1,2,3} Jesús Carrete², Zhenzhen Feng,^{1,4} Shuping Guo²,^{1,3} Yongsheng Zhang²,^{1,3,*} and Georg K. H. Madsen^{2,*}¹Key Laboratory of Materials Physics, Institute of Solid State Physics, HFIPS, Chinese Academy of Sciences, Hefei 230031, China²Institute of Materials Chemistry, TU Wien, A-1060 Vienna, Austria³Science Island Branch of Graduate School, University of Science and Technology of China, Hefei 230026, China⁴Institute for Computational Materials Science, School of Physics and Electronics, Henan University, Kaifeng 475004, China (Received 17 January 2020; revised 9 July 2020; accepted 30 August 2020; published 29 September 2020)

We calculate the lattice thermal conductivities of the pyrite-type ZnSe₂ at pressures of 0 and 10 GPa by using the linearized phonon Boltzmann transport equation. We obtain a very low value (0.69 W/mK at room temperature at 0 GPa), comparable to the best thermoelectric materials. The vibrational spectrums are characterized by the isolated high-frequency optical phonon modes due to the stretching of Se-Se dimers and the low-frequency optical phonon modes with a strong anharmonicity due to the rattling modes of Zn atoms, especially the rotations of Zn atoms around these dimers. This means that the existence of localized Se-Se dimers leads to the strong anharmonicity of the low-frequency optical phonon modes. Interestingly, two transverse acoustic phonon modes with similar frequencies and wave vectors have very different degrees of anharmonicity. We show that the anharmonicities of the transverse acoustic phonon modes are connected to the corresponding changes in the pyrite parameters. Furthermore, to determine the thermoelectric performances of ZnSe₂, we also investigate its electrical transport properties. Our results show that both *p*-type and *n*-type ZnSe₂ can possess promising electrical transport properties contributed by the complex energy isosurfaces of both valence and conduction bands. The low thermal conductivities and promising electrical transport properties lead to a large thermoelectric figure of merit of ZnSe₂ for both *p*-type and *n*-type doping at different pressures. Our study reveals the effect of the localized nonmetallic dimers on the anharmonicity and lattice thermal conductivity in the pyrite-type compound, which can be used to guide researchers to seek promising thermoelectric materials containing nonmetallic dimers.

DOI: [10.1103/PhysRevB.102.125204](https://doi.org/10.1103/PhysRevB.102.125204)**I. INTRODUCTION**

Thermoelectric (TE) materials can generate electricity from waste heat. They therefore have the potential to play an important role in solving the current energy and environmental crisis. The thermoelectric conversion efficiency is determined by the dimensionless thermoelectric figure of merit $ZT = S^2\sigma T/\kappa$, where T is the absolute temperature, S is the Seebeck coefficient, σ is the electrical conductivity, and κ is the thermal conductivity comprising both electronic (κ_e) and lattice (κ_l) contributions. The larger ZT value, the greater is the maximum achievable thermoelectric conversion efficiency. Based on the definition of ZT , the promising thermoelectric materials benefit from a large power factor ($PF = S^2\sigma$) and a low κ . However, it is very difficult to simultaneously achieve large electrical transport coefficients (S and σ) and low κ in a compound, since S , σ , and κ_e are carrier concentration dependent and therefore correlated with each other [1]. Many methodologies have been used to enhance phonon scattering and decrease the lattice thermal conductivity, such as introducing defects, impurities, boundaries and nanostructures, etc. However, these methodologies can also impede

charge carrier transport [2]. As a result, the current promising TE materials are limited to few compounds, such as, SiGe [3,4], PbTe [5–7], Bi₂Te₃ [8,9], Skutterudites [10–12], Clathrates [13,14] and Half-Heusler [15–17] compounds, etc. And the state-of-the-art TE materials usually contain toxic or nonabundant chemical elements (such as Pb and Te), and have relatively low ZT values, resulting in low energy conversion efficiency [18]. This limits the commercial application of TE devices and makes the quest for new TE materials with promising thermoelectric performances still ongoing.

Recently, we have investigated the thermoelectric properties of 243 known binary semiconductor chalcogenides using high-throughput computations, and predicted some high-performance TE materials with promising electrical transport property and strong anharmonicity [19]. Among them, the dichalcogenide ZnSe₂ interested us because of its simple crystal structure and abundant elements. In 1968, ZnSe₂ was successfully synthesized at high pressure (6.5 GPa) and high temperature (600–800 °C), and found to be (meta-)stable at room temperature and ambient pressure [20]. Therefore, ZnSe₂ deserves further attention both to clarify its transport properties using more accurate quantitative predictive methods and to understand the physical mechanisms behind its strong anharmonicity and promising thermoelectric behavior.

In this work, using first-principles calculations, we study the phase stabilities of ZnSe₂ at different pressures. We find

*Corresponding authors: yshzhang@theory.issp.ac.cn; georg.madsen@tuwien.ac.at

that ZnSe₂ is mechanically stable at different pressures. Solving the full linearized phonon Boltzmann transport equation (BTE), we calculate the lattice thermal conductivities of ZnSe₂ at 0 and 10 GPa. Our results show that ZnSe₂ has a very low lattice thermal conductivity. It is due to the existence of localized Se-Se dimers which can contribute to the strong anharmonicity of the rattling Zn atoms, and the existence of one of the transverse acoustic phonon branches with a strong anharmonicity caused by the strong local change of the pyrite parameter. Based on the electron BTE and the deformation potential approach, we find that both *p*-type and *n*-type ZnSe₂ exhibit promising electrical transport properties, which is due to the complex energy isosurfaces of both valence and conduction bands. Combining the low thermal conductivities and promising electrical transport properties, we find that ZnSe₂ is an excellent thermoelectric material for both *p*-type and *n*-type doping at different pressures.

II. COMPUTATIONAL METHODOLOGIES

A. Density functional theory calculations

The electronic structure of ZnSe₂ is calculated utilizing density functional theory (DFT) as implemented in the Vienna *ab initio* simulation package (VASP) [21] with the projector augmented wave (PAW) [22] method. The electronic exchange and correlation energy are accounted for the generalized gradient approximation of Perdew, Burke, and Ernzerhof (GGA-PBE) [23]. The energy cutoff for the plane-wave expansion is 420 eV. The geometry is relaxed until the change in total energy is less than 10⁻⁵ eV and the force components of each atom are below 0.01 eV/Å. The Brillouin zone is sampled using a (6×6×6) Monkhorst-Pack *k*-point mesh [24]. Since the GGA is well-known for underestimating the band gaps of semiconductors and insulators, we further carry out calculations with the Heyd-Scuseria-Ernzerhof functional (HSE06) [25,26] to achieve the more accurate band gap of ZnSe₂.

The phonon vibrational properties are calculated using the finite displacement method, as implemented in the PHONOPY software package [27]. To obtain reliable phonon dispersions, we need a highly optimized crystal structure. Thus, a (6×6×6) *k*-point mesh, a 10⁻⁸ eV energy convergence criterion and a 10⁻⁴ eV/Å force convergence criterion are adopted to further optimize the crystal structure of ZnSe₂, and a (2×2×2) supercell with 96 atoms is used. In the quasi-harmonic DFT phonon calculations, the crystal volumes are isotropically changed by ±3% based on the DFT relaxed volume.

The lattice thermal conductivities (κ_l) are calculated by solving the full linearized phonon BTE as implemented in the almaBTE code [28]. In the almaBTE method, the Born effective charges and the dielectric tensors are calculated using VASP. To determine the amplitudes of the three-phonon processes, the third-order interatomic force constants are computed using the thirdorder.py code [29]. We consider interatomic interactions up to the seventh coordination shell. And a (10×10×10) Γ -centered grid is used to solve the phonon BTE.

B. Electrical transport property calculations

The electrical transport properties (S , $\frac{\sigma}{\tau}$, and κ_e) are calculated using the BoltzTraP2. Code [30], which is based on the electron BTE. A highly dense (35×35×35) *k*-point mesh is used to obtain accurate electrical transport properties. Since the wavelength of a thermal electron is comparable with the lattice constant, the acoustic phonon scattering is typically the dominant carrier scattering mechanism [31]. We therefore model the average carrier relaxation time by considering the acoustic phonon scattering mechanisms using the deformation potential approach. In the approach, the carrier relaxation time of a single energy valley (τ_i) can be given from the single parabolic band model, as [31]

$$\tau_i = \frac{2^{\frac{1}{2}} \pi \hbar^4 \rho v_{LA}^2}{3E_{di}^2 (m_{bi}^* k_B T)^{\frac{3}{2}}} \frac{F_0(\eta)}{F_{\frac{1}{2}}(\eta)},$$

$$F_x(\eta) = \int_0^\infty \frac{E^x}{1 + \exp(E - \eta)} dE, \quad \eta = \frac{\mu}{k_B T}, \quad (1)$$

where \hbar is the reduced Planck constant, k_B is the Boltzmann constant, ρ is the mass density, v_{LA} is the longitudinal acoustic (LA) phonon velocity, η is the reduced chemical potential, m_{bi}^* and E_{di} are the single valley density of states (DOS) effective mass (m_b^*) and the deformation potential (E_d) of the i^{th} valley. For a semiconductor with degenerate valleys [32], considering the detrimental effect of the multivalley scatterings on electrical properties, the relationship between the carrier relaxation time (τ) and the energy valley degeneracy (N_V) can be expressed as $\tau \propto \frac{1}{N_V}$. Based on the relationship, assuming that the scattering mechanisms of different single valley scatterings are independent, the total carrier relaxation time (τ) can be evaluated from the individual relaxation times as

$$\frac{1}{\tau} = \sum_i \frac{D_i}{\tau_i}, \quad (2)$$

where D_i is the symmetry degeneracy of the i^{th} valley, and the relationship between N_V and D_i is $N_V = \sum_i D_i$. Furthermore, to consider the anisotropy, m_b^* can be obtained from the geometric mean effective mass of a single equivalent ellipsoid energy valley, as [33]

$$m_b^* = (m_{\parallel}^* m_{\perp}^{*2})^{\frac{1}{3}}, \quad (3)$$

where m_{\parallel}^* and m_{\perp}^* are the principal effective masses parallel and perpendicular to the long axis of the elliptic energy valley, respectively. They can be calculated from the band structures as

$$m_{\parallel/\perp} = \hbar^2 \left[\frac{\partial^2 E(k)}{\partial k_{\parallel/\perp}^2} \right]^{-1}. \quad (4)$$

And v_{LA} can be calculated from the weighted averages of the particular LA phonon velocity ($v_{LA}^{\alpha\beta}$) along (α, β) wave vector as

$$v_{LA} = \frac{1}{\sum_{\alpha\beta} D_{\alpha\beta}} \sum_{\alpha\beta} D_{\alpha\beta} v_{LA}^{\alpha\beta}, \quad (5)$$

$$v_{LA}^{\alpha\beta} = \frac{\partial \omega_{LA}^{\alpha\beta}}{\partial k_{\alpha\beta}}, \quad (\alpha, \beta = x, y, z), \quad (6)$$

where, $D_{\alpha\beta}$, $k_{\alpha\beta}$, and $\omega_{LA}^{\alpha\beta}$ are the symmetry degeneracy, the reciprocal space wave vector, and the LA phonon frequency along the (α, β) direction, respectively. The deformation potential characterizes the changes in carrier energies with per unit elastic strain. In our work, to evaluate the averaged electron relaxation time, we use the simple volume deformation potential (E_d) defined as

$$E_d = \frac{\Delta E}{\frac{\Delta V}{V}}, \quad (7)$$

where ΔE is energy change of the band extrema of the single energy valley [the valence band maximum (VBM) or the conduction band minimum (CBM)] with the volume dilation $\frac{\Delta V}{V}$. To calculate E_d , the crystal volumes are isotropically changed from -4% to 4% , and considering the energy of the deep core level is hardly affected by such small volume variations and choosing the deep level as the reference level. The deformation potential approach has been successfully applied to predict ZT values in a number of investigations of the thermoelectric materials [34–37].

It needs to be noted that the deformation potential approach cannot include the effects of intervalley, impurity, and other scatterings on the electronic relaxation time. The intervalley scatterings would have an impact on the transport properties in degenerate semiconductors. However, there is no simple way of incorporating the intervalley scattering in the deformation potential methodology. Additionally, from the previous study [38], the authors found that the intervalley contributes little to the total scatterings in lead chalcogenides. Therefore, we neglect the effect in the current work. Furthermore, in the doped semiconductors, the impurity scatterings will obviously affect the electron transport properties. However, the scattering mechanism is complicated and out of the range of the current work.

III. RESULTS AND DISCUSS

A. Crystal structure and stability of ZnSe₂

The dichalcogenide ZnSe₂ with a pyrite-type crystal structure [Fig. 1(a)] was synthesized at 6.5 GPa and found to be (meta-)stable at ambient pressure in 1968 [20]. The pyrite-type ZnSe₂ is a cubic structure (space group Pa $\bar{3}$) with Wyckoff position 4a(0,0,0) for Zn and 8c(u,u,u) for Se, where

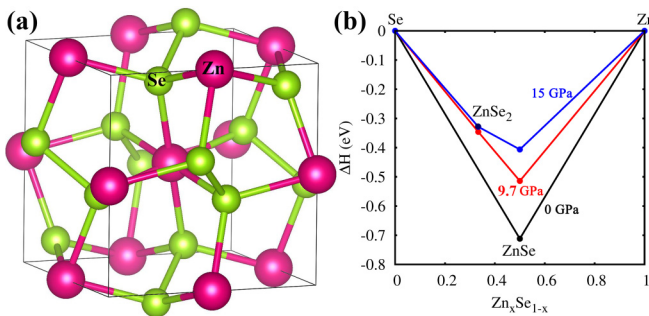


FIG. 1. (a) The pyrite-type crystal structures of ZnSe₂ (space group Pa $\bar{3}$). (b) DFT calculated pressure-composition phase diagrams of Zn_xSe_{1-x} at 0 (black), 9.7 (red), and 15 (blue) GPa, respectively.

u is the pyrite parameter. In the structure, each Zn has six Se as nearest neighbors and each Se has three Zn and one Se as nearest neighbors. In this work, our relaxed lattice constant (6.366 Å) at 0 GPa is larger than the experimental (6.293 Å) [20], as is typically found for the PBE functional. And the calculated bond lengths of Zn-Se (L_{Zn-Se}) and Se-Se (L_{Se-Se}) are 2.68 and 2.40 Å at 0 GPa.

To check the thermodynamic stability of ZnSe₂ under pressures, we calculate the formation enthalpy [$\Delta H(P)$] of Zn_xSe_{1-x} at different pressures,

$$\Delta H(P) = H(\text{Zn}_x\text{Se}_{1-x}) - xH(\text{Zn}) - (1-x)H(\text{Se}), \quad (8)$$

where x is the composition of Zn in the Zn-Se compound, and $H(=E + PV)$ is the pressure dependent enthalpy at different pressures (P) and volumes (V). We calculate the formation enthalpies of Se, ZnSe, ZnSe₂, and Zn for different phases [39] in the pressure range from 0 to 15 GPa and setup the pressure-composition phase diagrams of Zn_xSe_{1-x} [Figs. 1(b) and S1(a) in the Supplemental Material [40] in detail]. At 0 GPa, we find that ZnSe (the zincblende phase) is thermodynamically stable. However, the formation enthalpy of ZnSe₂ is only ~ 0.14 eV above the convex hull, which could indicate that ZnSe₂ is a metastable compound. Additionally, due to pressure having a stronger influence on the formation enthalpy in ZnSe than in ZnSe₂: increasing pressure from 0 to 15 GPa, the formation enthalpy increases ~ 0.306 eV in ZnSe, while only ~ 0.001 eV in ZnSe₂. And the differences in the formation enthalpies between ZnSe₂ and Se+ZnSe $\Delta H = H(\text{ZnSe}_2) - H(\text{Zn}) - H(\text{ZnSe})$ as a function of pressure are shown in Fig. S1(b) in the Supplemental Material [40]. As a result, ZnSe₂ becomes a thermodynamically stable compound at pressure higher than 9.7 GPa. The predicted pressure (9.7 GPa) is in reasonable agreement with the synthesis pressure (6.5 GPa) [20]. This slight pressure difference between theoretical calculation and experimental measurement may be due to the fact that ZnSe₂ was synthesized under the combination of pressure and temperature, while in our theoretical study, the calculated formation enthalpy only considers the influence of pressure not temperature.

Because the theoretically predicted pressure induced thermodynamically stability of ZnSe₂ is 9.7 GPa, we calculate the geometric, vibrational, and electrical properties of ZnSe₂ at 10 GPa. At 10 GPa, the lattice constant (a) of ZnSe₂ shrinks to 6.102 Å, and the calculated L_{Zn-Se} and L_{Se-Se} are compressed to 2.56 and 2.36 Å. Compared to the calculated interatomic bond lengths at 0 GPa, it is clear that L_{Zn-Se} (0.12 Å) is changed substantially more than L_{Se-Se} (0.04 Å).

In order to study the mechanical stability of ZnSe₂, we calculate the phonon dispersions of ZnSe₂ at 0 [Fig. 2(a)] and 10 GPa [Fig. 2(c)]. From Fig. 2, we find that all phonon frequencies are real, which indicates that ZnSe₂ is mechanically stable both under and at ambient pressures. The stable phonon behavior of ZnSe₂ at 0 GPa underlines that even though the compound is synthesized at high pressure, it should be metastable at ambient pressure. At 0 GPa, the phonon density of states (PDOS) of per atom of ZnSe₂ is shown in Fig. 2(b). The most striking thing is the presence of the localized high-frequency phonon modes at $\omega \approx 250$ cm⁻¹, which are almost entirely made up of Se vibrations.

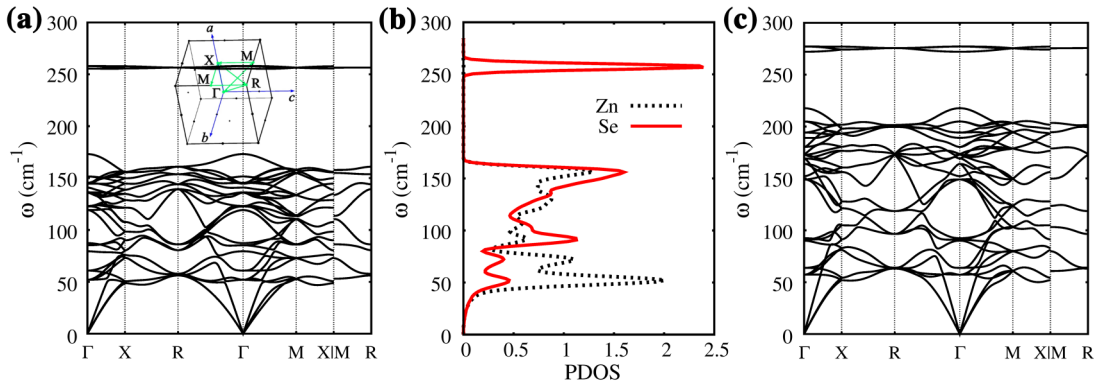


FIG. 2. Phonon dispersions of ZnSe_2 at 0 (a) and 10 GPa (c). The first Brillouin zone of ZnSe_2 with the high-symmetry points is illustrated as an inset in (a). (b) The corresponding phonon density of states (PDOS) of per atom in ZnSe_2 at 0 GPa.

To understand the origin of these high-frequency phonon modes and further illustrate the bonding situation in ZnSe_2 , we calculate the electron localization function (ELF) [41]. The ELF measures the extent of spatial localization of the reference electron located at a given position, with values ranging from 0 to 1. $\text{ELF} = 0.5$ corresponds to the electron gas, while $\text{ELF} = 1$ corresponds to perfect localization (as found in regions with covalent bonds, core shells, and lone pairs) [41]. Figures 3(a) and 3(b) show the calculated three-dimensional (3D) and projected 2D [in (001) plane] ELF of ZnSe_2 at 0 GPa, respectively. From Fig. 3(a), we notice that there is a dumbbell ELF shape around the Se-Se bond. The dumbbell shape can be interpreted as the presence of Se-Se dimers connected by the strong covalent bond. A detailed analysis of the phonon dispersions reveals that the stretching of Se-Se bonds in the dimers contributes to the localized high-frequency phonon modes at $\omega \approx 250 \text{ cm}^{-1}$ (as shown in Fig. S2 in the Supplemental Material [40]).

To further understand the vibrational properties of different atoms, we calculate atomic displacement parameters (ADPs, the mean squared displacement amplitude of the atom relative to its equilibrium position) of Zn and Se atoms along different directions, as shown are in Fig. 3(c). The ADPs of Zn atoms are much larger than that of Se atoms, indicating that Zn atoms are more loosely bound and behave as rattling atoms [35]. This agrees well with the change of $L_{\text{Zn-Se}}$ being greater than that of $L_{\text{Se-Se}}$ at 10 GPa and the low-frequency optical phonons ($40 \text{ cm}^{-1} < \omega < 80 \text{ cm}^{-1}$) having larger Zn than Se contributions, Fig. 2(b), despite the lower mass of Zn.

B. Low lattice thermal conductivities

In our previous high-throughput work [19], we predicted that ZnSe_2 could possess a low lattice thermal conductivity (κ_l). The prediction was based on a strong dependence of the elastic properties on volume, which could indicate a strong anharmonicity or, more specifically, a large Grüneisen parameter (γ). In this work, we explicitly calculate the thermal conductivity using the full linearized phonon BTE coupled with DFT, which is well known for quantitative predictive power [42–45]. Specifically, we calculate κ_l at both 0 and 10 GPa, as shown in Fig. 4, and find that ZnSe_2 has a very low lattice thermal conductivity: κ_l is equal to 0.69 and 1.98 W/mK at 300 K at 0 and 10 GPa, respectively. These values are comparable to the known low-thermal conductivity compounds for thermoelectric applications, such as SnSe [46] and PbTe [47] (the measured lattice thermal conductivities of the two compounds are 0.45–0.7 and 2.4 W/mK at room temperature, respectively).

To verify the applicability of the phonon BTE to a situation with such low thermal conductivities, we calculate the minimum lattice thermal conductivity (κ_{\min}) from

$$\kappa_{\min} = \frac{1}{3} \sum_q C_q v_q \frac{v_q}{\omega_q}, \quad (9)$$

where C_q (J/m³K) is the contribution of each phonon to the volumetric heat capacity. This value approximates the thermal conductivity that the system would display if every phonon has a mean free path that put it at the Ioffe-Regel crossover, below which the phonon-based description is no longer useful

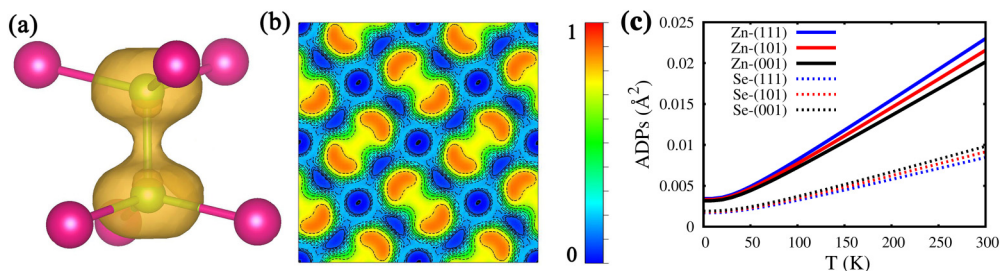


FIG. 3. (a) 3D electron localization function (ELF) of ZnSe_2 at 0 GPa. The ELF value of the isosurface is 0.7. (b) Projected 2D ELF in (001) plane of ZnSe_2 at 0 GPa. (c) Calculated atomic displacement parameters (ADPs) of Zn and Se atoms along different directions.

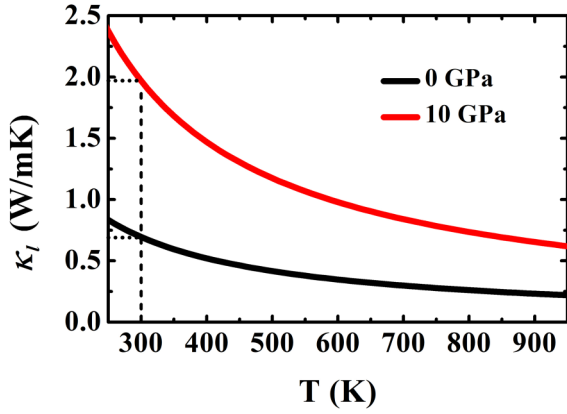


FIG. 4. Calculated κ_l of ZnSe_2 as a function of temperature at 0 and 10 GPa, respectively.

[48]. The calculated κ_{\min} , 0.09 and 0.10 W/mK at 300 K at 0 and 10 GPa, are well below κ_l in Fig. 4, lending support to our choice of the formalism.

C. Strong anharmonicity

The mode dependent Grüneisen parameters ($\gamma_{iq} = -\frac{V}{\omega_{iq}} \frac{\partial \omega_{iq}}{\partial V}$) can be viewed as weighted averages of the third-order force constants which enter the expression for the scattering rates [49]. Several previous studies have linked a large Grüneisen parameter (strong anharmonicity) with a low thermal conductivity [46,50–59]. To investigate the origins of the low κ_l of ZnSe_2 , we evaluate γ_{iq} on a mode-by-mode basis by calculating the change of the phonon vibrational properties (ω_{iq}) when the volume of system is isotropically changed by $\pm 3\%$ with respect to the DFT relaxed volume at 0 GPa. The calculated γ_{iq} at different phonon modes are shown in Fig. 5(a). From Fig. 5(a), we find that many low-frequency phonon modes ($\omega < 150 \text{ cm}^{-1}$) have strong anharmonicities ($\gamma > 2$) and the maximum Grüneisen parameter located at one of the transverse acoustic phonon branches (TA) is 4.6, which is comparable to the well-known SnSe compound with strong anharmonicity ($\gamma_a = 4.1$, $\gamma_b = 2.1$, and $\gamma_c = 2.3$ along the \vec{a} , \vec{b} , and \vec{c} three directions, respectively) [60].

Through computing the κ_l contribution for ZnSe_2 with respect to phonon frequency at 300 K [Fig. 5(b)], we find

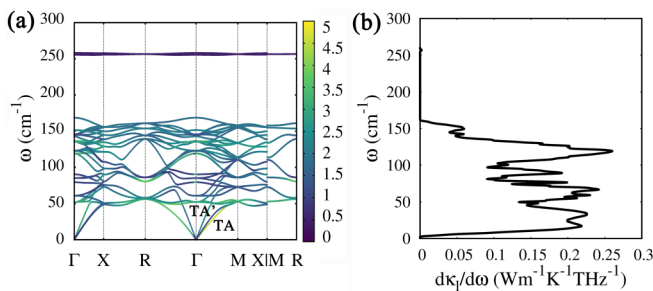


FIG. 5. (a) The phonon dispersions and the corresponding distributions of γ_{iq} in ZnSe_2 at 0 GPa. The color in (a) denotes the values of γ_{iq} . (b) The κ_l contribution with respect to phonon frequency at 300 K.

that the high-frequency phonons contributed by Se-Se dimers ($\omega \sim 250 \text{ cm}^{-1}$) make almost no contribution to the thermal conductivity. Instead, the thermal conductivity has contributions from a rather broad frequency window with $\omega < 150 \text{ cm}^{-1}$. Interestingly there is a drop in the frequency resolved thermal conductivity at around 50 cm^{-1} , where low lying optical phonon modes are present. The effect of these low-lying optical modes on the thermal conductivity will be twofold. First of all, they will open up scattering channels similar to the “rattler” of, e.g., the skutterudites [61]. Secondly, the Grüneisen parameter is large for these modes indicating a strong anharmonicity. Additionally, these localized modes can be a large degree associated with the motions of Zn atoms [Fig. 2(b)]. A detailed analysis of these vibrations reveals that they are mainly made up of the motions of Zn rotations around Se-Se dimers [as shown in Fig. 6(a) as an inset]. This indicates that the localized Se-Se dimers are bonded to the neighboring Zn atoms which perform an anharmonic librational like motions around the Se-Se dimers. In Fig. 6(a), the contribution of the Zn rotational motions to the phonon dispersions around 50 cm^{-1} is shown.

A further striking feature in Fig. 5(a), is that the Grüneisen parameters of certain acoustic bands are quite large. Consequently, it is also observed that the acoustic phonons make a surprising small overall contribution to the thermal conductivity, Fig. 5(b), which will be an important factor in the overall low thermal conductivity. In particular, one of the transverse acoustic phonon branches (TA) along the ΓM high-symmetry direction has very large Grüneisen parameters ($\gamma > 4$), whereas another transverse acoustic phonon branch (TA') along the same direction has low γ ($\gamma < 2$). This is a remarkable contrast that deserves further investigation, since whatever factor is behind the very different anharmonicities of these two branches may also help to better explain the anharmonicity character of the crystal as a whole.

As opposed to the localized Zn-rotation modes mentioned above, the TA and TA' phonon branches cannot be attributed to a localized vibration mode of the specific atom type, but are contributed by the vibration modes of all atoms along the same direction. Instead we characterize them by the pyrite parameter (u) which determines the nonmetal atom positions in a given pyrite-type crystal [62]. When the whole crystal vibrates according to a particular acoustic phonon mode, the parameter changes locally for relatively large volumes of the

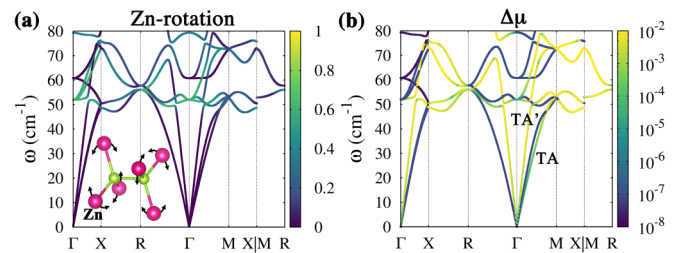


FIG. 6. (a) The contribution of the motions of Zn rotations around Se-Se dimers to the phonon dispersions around 50 cm^{-1} . The motion of Zn rotations around Se-Se dimers vector is illustrated as an inset in (a). (b) The distribution of the changed pyrite parameters (Δu) at the acoustic phonons.

crystal. Hence, for a given unit cell, an acoustic phonon vibration which changes the pyrite parameter acts similarly to an expansion or contraction. This, as we have already discussed, must trigger a large change to the TA phonon dispersion because of the significant anharmonicity and consequential large Grüneisen parameter. For the purposes of this work, we evaluate the linear sensitivity of the pyrite parameter (Δu) to each phonon mode by means of the following quantity:

$$\begin{aligned} \langle (u - u_0)^2 \rangle_H &= \int_0^1 \{u[r_0 + H \times (\mathcal{R}\{v\}\cos(2\pi s) \\ &\quad + \mathcal{I}\{v\}\sin(2\pi s))] - u_0\}^2 ds, \\ \Delta u &= \lim_{H \rightarrow 0} \frac{\sqrt{\langle (u - u_0)^2 \rangle_H}}{H}, \end{aligned} \quad (10)$$

where $\mathcal{R}\{v\}$ and $\mathcal{I}\{v\}$ are the real and imaginary part of the phonon eigenvector (v), respectively, u_0 is the pyrite parameter of the pristine cell, and the value of $u(r)$ is calculated by fitting the coordinates to those of a pyrite unit cell in a least-squares sense. The calculated Δu for the acoustic phonons are shown in Fig. 6(b). From Fig. 6(b), it becomes apparent that Δu is significantly larger for the TA branch than for the TA' branch along the Γ M high-symmetry line. This means that the large γ at the TA phonon region can be explained in terms of the sensitivity of the pyrite parameter to different vibrational modes.

Owing to the above analysis, the strong anharmonicity comes from two parts: (1) the low-frequency optical phonons contributed by the rattling modes of Zn atoms, especially the rotations of Zn atoms around the Se-Se dimers, and (2) the TA phonons caused by the large local changes of the pyrite parameters. Furthermore, the strong anharmonicity of ZnSe₂ is related to the localized Se-Se dimers and could lead to the low lattice thermal conductivity (0.69 W/mK at 300 K) at 0 GPa. As mentioned above, comparing with 0 GPa, the interatomic bond lengths ($L_{\text{Zn-Se}}$ and $L_{\text{Se-Se}}$) are compressed at 10 GPa, resulting in an enhancement of the interatomic interactions and the higher-frequency phonon dispersions [as shown in Fig. 2(c)]. Therefore, despite ZnSe₂ also has the

large Grüneisen parameters at 10 GPa (Fig. S3 in the Supplemental Material [40]), it is reasonable and easy to understand that κ_l is increased to 1.98 W/mK at 300 K.

D. Promising electrical transport properties

After calculating the lattice thermal conductivity, we investigate the electrical properties of ZnSe₂. The calculated electronic band structures at 0 GPa by PBE is shown in Fig. 7(a). Since PBE is well known to underestimate the band gap of semiconductor [23], we also calculate the electronic band structures of ZnSe₂ at 0 GPa using HSE06 [Fig. 7(b)]. From the two band structures [Figs. 7(a) and 7(b)], we find that the band gaps are 0.72 and 1.62 eV using PBE and HSE06, respectively. Fortunately, the band features around the Fermi level (valence bands and conduction bands) are similar in the two functional calculations. Therefore, we do not carry out the time-consuming HSE06 calculations with a highly dense k -point mesh for the electron BTE. Instead, we use the PBE electronic band structures and simply manually increase the band gap. At 10 GPa, the PBE calculated band gap is 0.61 eV [Fig. 7(c)]. Assuming that the difference of the band gap (0.9 eV) using PBE and HSE06 does not change with pressure, we can set the band gap of ZnSe₂ at 10 GPa to ~ 1.51 eV.

The band behavior is further illustrated by the energy isosurfaces at 0 GPa as shown in Fig. 8. The energy valleys of conduction and valence bands in Fig. 8 relate to the corresponding energy band extrema in Fig. 7(a). From the band structures and energy isosurfaces of ZnSe₂ [Figs. 7(a) and 8(a)], we find the valence band maximum (VBM) and the secondary VBM (VBM2) are located at Γ (VBM- Γ) and X (VBM2-X) points, respectively, and VBM- Γ and VBM2-X both have a twofold band-degeneracy. The energy difference between VBM- Γ and VBM2-X is small (0.15 eV), which is comparable to that in the well-studied PbTe [63]. The small energy difference means VBM- Γ and VBM2-X both will fall within the width of the fermi distribution function and contribute to the electrical transport properties. From Fig. 8(a), we notice that VBM-B1 has a large anisotropic isosurface, which means that p -type ZnSe₂ possesses both light and heavy

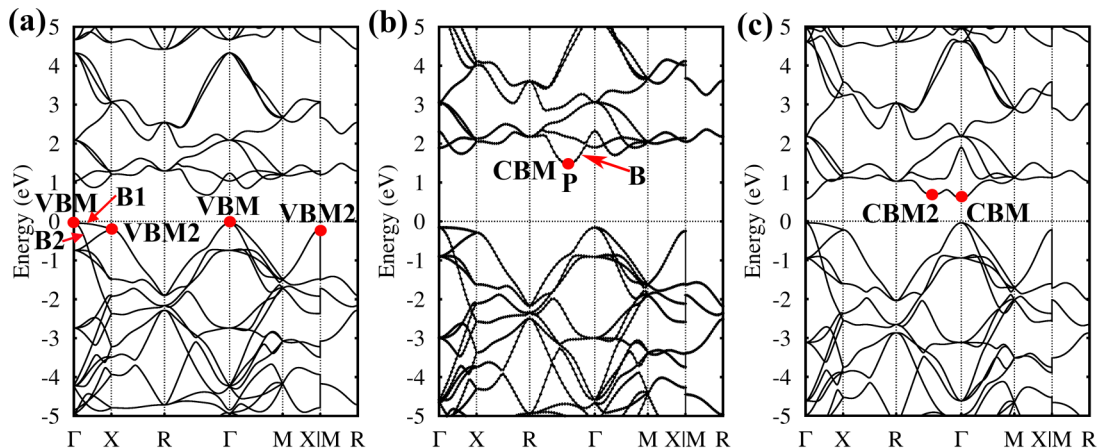


FIG. 7. Calculated band structures of ZnSe₂ at 0 GPa for (a) PBE and (b) HSE approximations. (c) is the calculated K band structures of ZnSe₂ at 10 GPa for PBE approximation.

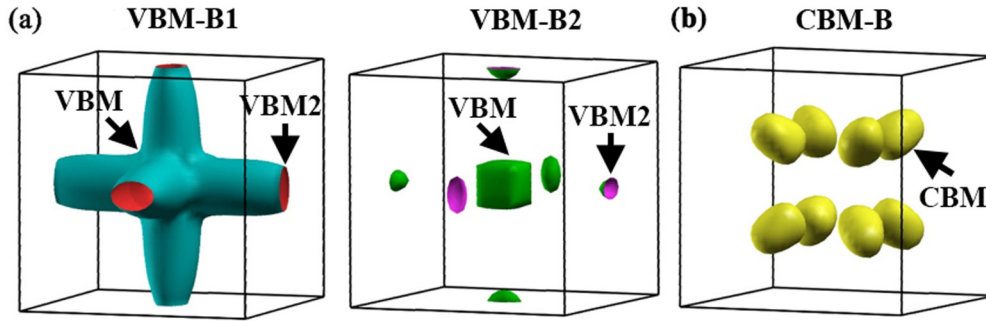


FIG. 8. The energy isosurfaces at 0.2 eV low VBM (a) and 0.15 eV above CBM (b) of ZnSe_2 at 0 GPa.

carriers depending on direction. The corresponding carrier effective masses ($m_{\alpha\beta}^* = \hbar^2 [\frac{\partial^2 E(k)}{\partial k_\alpha \partial k_\beta}]^{-1}$) along different directions are listed in Table S1 in the Supplemental Material [40]. The light carriers can contribute the large σ , while the heavy carriers can facilitate the large S . Moreover, in a cubic structure, the symmetry degeneracy of VBM2-X is three. Combining the twofold band degeneracy of VBM- Γ and VBM2-X means that p -type ZnSe_2 has a large total valley degeneracy (eight). The large anisotropic isosurface and the large valley degeneracy indicate the complex energy isosurfaces [33], which would suggest the promising electrical properties of p -type ZnSe_2 . From the band structures of ZnSe_2 at different pressures [0 and 10 GPa, Figs. 7(a) and 7(c)], we notice that the valence band features are almost unaffected under pressures, such as, the positions of VBM and VBM2 and the shapes of B1 and B2 do not change with pressures. However, the energy difference between VBM- Γ and VBM2-X is slightly increased from 0.15 to 0.18 eV, which will result in small changes in the electrical properties of p -type ZnSe_2 at high pressure.

For the conduction bands, the conduction band minimum (CBM) is located along Γ -R direction [the P point in Fig. 7(b), CBM-P] at 0 GPa, the symmetry degeneracy of CBM-P is eight and the energy isosurfaces are complex, as shown in Fig. 8(b). With increasing pressure to 10 GPa, the band features of conduction bands are significantly changed: one band at Γ point significantly lowers and becomes the CBM (CBM- Γ), while the band at the P point becomes the secondary conduction band minimum (CBM2-P). The energy difference between CBM- Γ and CBM2-P at 10 GPa is small (0.12 eV). The shift of CBM results in the valley degeneracy of n -type ZnSe_2 to increase from eight to nine at 10 GPa. From Fig. 8(a), the shapes of CBM-P are nearly spherical, which means that the carriers of n -type ZnSe_2 along different directions will have similar effective masses. Consistent with the discussion above, from Table S1 in the Supplemental Material [40], we find that the carriers at CBM (CBM-P at 0 GPa, CBM- Γ and CBM2-P at 10 GPa) have similar and small $m_{\alpha\beta}^*$ (smaller than the mass of a free electron) along different directions. The large valley degeneracy (the complex energy isosurfaces) and small effective masses of CBM suggest that n -type ZnSe_2 also can possess the promising electrical properties at different pressures.

To further investigate the electrical properties of ZnSe_2 near Fermi level, we analyze the bonding characteristics at 0 GPa [Fig. 9(a)]. The bonding characteristics are estimated using the LOBSTER package [64–67] to calculate the projected

crystal orbital Hamilton population (COHP). The negative and positive COHP values indicate the bonding and antibonding characters between atom pairs, respectively. Interestingly, the top of valence bands ($E < E_f$) and both the bottom of conduction bands ($E > E_f + E_g$) are dominated by states with an antibonding character of Zn-Se and Se-Se. While it is somewhat unusual that the top of valence bands has an antibonding character, it is interesting to note that a similar feature has previously been found in materials with a complex conduction band edge dominated by several carrier pockets [68]. Moreover, through analyzing the projected band structures of ZnSe_2 [Fig. 9(b)], we find that the valence bands are mainly contributed by the electronic states of Zn_d and Se_p , and the conduction bands are mainly contributed by the electronic states of Zn_s and Se_p . For the valence bands, the weights of the same electronic states (Zn_d or Se_p) at different bands are very similar. However, for the conduction bands, the electronic states in the first conduction band (CBM) are contributed by Zn_s and Se_p together, while the the electronic states in second conduction band (CBM2) are contributed by Se_p solely. We thus infer that the electronic states in CBM at P point (CBM-P) are contributed by the antibonding states of Zn_s - Se_p and Se_p - Se_p together, while the electronic states in CBM2 at Γ point (CBM2- Γ) are only contributed by the antibonding states of Se_p - Se_p . The change of the relative bonding strength between Zn-Se and Se-Se will result in the variation of the band energy difference between CBM-P and CBM2- Γ .

In order to calculate the electrical conductivities of ZnSe_2 , we need to estimate the carrier relaxation time, τ , from Eqs. (1) and (2), which requires the single DOS effective masses (m_b^*), the LA phonon velocities (v_{LA}), and the volume deformation potentials (E_d) of different valleys (at VBM and CBM). Based on Eqs. (3)–(7), we can calculate m_b^* , v_{LA} , and E_d from the electronic band structures [Eqs. (3) and (4)], the phonon dispersions [Eqs. (5) and (6)] and the electronic energy changes of the band extrema with volume [Eq. (7)], respectively. The values of m_b^* , v_{LA} , and E_d at different valleys at 0 and 10 GPa are given in Table I. In a semiconductor, the symmetry of the band extrema will define the number of deformation potentials needed to describe the scattering processes. In ZnSe_2 , the CBM at 0 GPa is located at the P point, which is not a high-symmetry point. The validity of the calculated E_d of CBM is verified by comparing it to the six independent deformation potentials (Ξ_{ij}) along six different strain tensors (S_{ij}) by using the definition of Ξ_{ij} as $\Delta E = \sum_{ij} \Xi_{ij} S_{ij}$ [69].

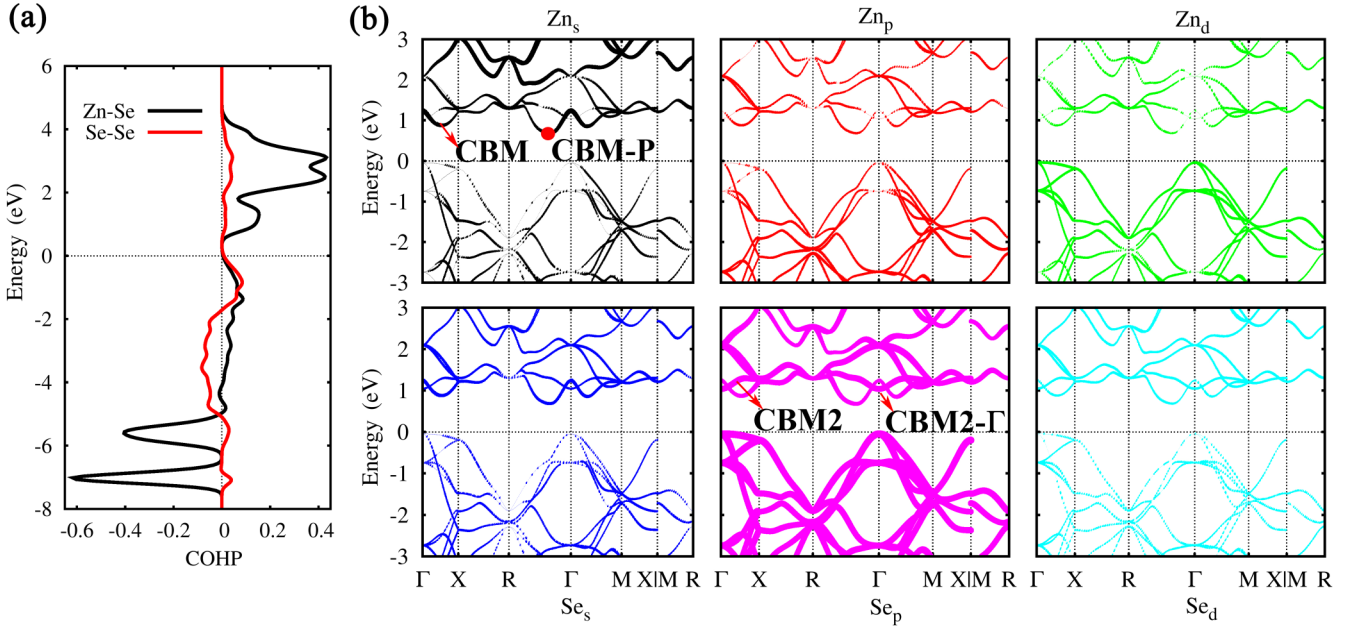


FIG. 9. (a) The orbital-resolved projected crystal orbital Hamilton population (COHP) of ZnSe_2 at 0 GPa. (b) The projected decomposed band structures of ZnSe_2 at 0 GPa. The thickness of the band feature represents the weights of the electronic state.

From Table I, we find that with increasing pressure from 0 to 10 GPa, v_{LA} is increased from 3684 to 4392 m/s, the calculated m_b^* of different valleys at VBM are slightly decreased, and the absolute values of E_d ($|E_d|$) at Γ and X points at VBM are slightly increased. From Eq. (1), for p -type ZnSe_2 , the increased v_{LA} and decreased m_b^* of VBM can lead to the increment of τ . However, due to the shift of CBM with pressure, the calculated m_b^* of CBM at the P point is drastically increased from $0.42m_0$ to $0.75m_0$ and $|E_d|$ of CBM at the P point is decreased. From Eqs. (1) and (2), for n -type ZnSe_2 , the increased m_b^* at the P point and the emergence of an energy valley at the Γ point of CBM can lead to the decrement of τ . The calculated τ of ZnSe_2 at 0 and 10 GPa are shown in Figs. 10(a) and 11(a), respectively. From them, we find that with increasing pressure, τ is increased for p -type doping, but decreased for n -type doping.

Polar optical phonon scattering could be important for an ionic material like ZnSe_2 at low carrier concentrations. [32,70] In order to investigate the validity of the deformation potential approach only considering acoustic phonon scattering, we calculate the relaxation times due to the polar optical

phonon scattering (τ_{po}) and compare them with the calculated relaxation times by only considering acoustic phonon scattering (τ) (shown in Fig. S4 in the Supplemental Material [40]). The results show that the contribution of the polar optical phonon scattering in ZnSe_2 is small. Therefore, we think that it is reasonable to only consider the acoustic phonon scattering effect in the relaxation time calculation. The detailed analyses and discussions are provided in the Supplemental Material [40].

Combining the calculated τ with the electron BTE, we obtain the corresponding electrical transport properties (S , σ , and PF) of p -type and n -type ZnSe_2 at different temperatures and carrier concentrations at 0 and 10 GPa, as shown in Figs. 10(b)–10(d) and 11(b)–11(d), respectively. Obviously, the increased carrier concentration deteriorates the Seebeck coefficient (S) but benefits the electrical conductivity (σ). Thus, the power factor ($PF = S^2\sigma$) reaches a maximum value (PF_{max}) at the carrier concentration around 10^{20}cm^{-3} at 300 K. From Figs. 10 and 11, we find that (1) both p -type and n -type ZnSe_2 have a high PF ($PF_{\text{max}} > 1.0\text{mW/mK}^2$) at different pressures, which are comparable with the best

TABLE I. Calculated longitudinal acoustic phonon velocity (v_{LA}), single DOS effective mass (m_b^*), and deformation potential (E_d) of different valleys at 0 and 10 GPa, respectively. m_0 is the mass of a free electron.

P (GPa)	v_{LA} (m/s)	$m_b^*(m_0)$				E_d (eV)				
		VBM		CBM		VBM		CBM		
		Γ	X	Γ	P	Γ	X	Γ	P	
		B1	B2							
0	3682	1.48	0.27	0.22	–	0.42	–10.0	–9.8	–	–11.4
10	4392	1.24	0.22	0.20	0.34	0.75	–11.6	–11.4	–7.5	–10.6

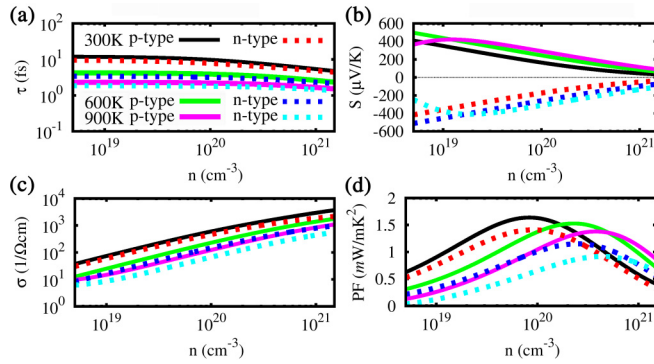


FIG. 10. Calculated τ (a), S (b), σ (c), and PF (d) of p -type and n -type ZnSe_2 as a function of the carrier concentration at 0 GPa, at 300, 600, and 900 K, respectively.

TE material (1.01 mW/mK^2 for SnSe) [46]. This means that ZnSe_2 does exhibit promising electrical properties for both p -type and n -type doping at different pressures. (2) The calculated PF_{max} is increasing for p -type ZnSe_2 but decreasing for n -type ZnSe_2 under pressure. This means that the pressure can be used to regulate the electrical transport properties of ZnSe_2 .

E. High ZT values

Based on the calculated τ , we can calculate the electronic thermal conductivities (κ_e) of ZnSe_2 using the BoltzTraP2 code [30]. The calculated κ_e of p -type and n -type ZnSe_2 at different temperatures and carrier concentrations are shown in Fig. S5 in the Supplemental Material [40]. Combining the calculated κ_l , κ_e , and PF of ZnSe_2 , we can evaluate ZT at different temperatures and carrier concentrations at 0 and 10 GPa, as shown in Figs. 12(a) and 12(b), respectively. At 0 GPa, the maximum ZT values of p -type and n -type ZnSe_2 can reach 2.21 and 1.87 at 900 K and at the carrier concentrations of 9.8×10^{19} and $1.6 \times 10^{20} \text{ cm}^{-3}$, respectively. The high ZT values indicate that ZnSe_2 is a promising thermoelectric material for both p -type and n -type doping. The comparative ZT values of p -type and n -type ZnSe_2 could be

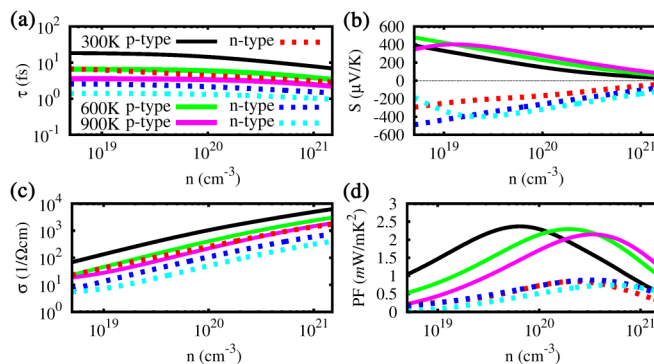


FIG. 11. Calculated τ (a), S (b), σ (c), and PF (d) of p -type and n -type ZnSe_2 as a function of the carrier concentration at 10 GPa, at 300, 600, and 900 K, respectively.

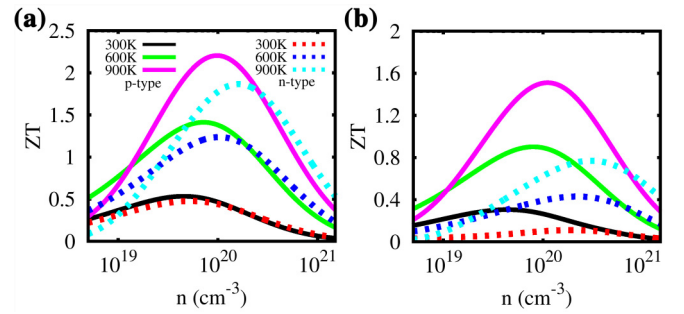


FIG. 12. Calculated ZT values of p -type and n -type ZnSe_2 as a function of temperature and carrier concentration at 0 (a) and 10 (b) GPa, respectively.

useful in designing two legs in the thermoelectric devices and also mean that, even if a doping limit should exist, at least either p -type or n -type ZnSe_2 can be realized. With increasing pressure to 10 GPa, since the increment of the electrical transport property (PF) is smaller than that of the lattice thermal conductivity (κ_l), the maximum ZT value of p -type ZnSe_2 is decreased to 1.51. Moreover, due to the decrement of PF and the increment of κ_l , the maximum ZT value of n -type ZnSe_2 is decreased to 0.77.

IV. CONCLUSION

In this work, based on the phonon and electron Boltzmann transport theories, we have systematically studied the thermoelectric performances of ZnSe_2 at different pressures. These results show that ZnSe_2 has both low lattice thermal conductivities and promising electrical transport properties at different pressures. Although the localized Se-Se dimers with strong covalent bond in ZnSe_2 result in the isolated high-frequency optical phonon modes, the weak interactions between the rattling Zn atoms with Se-Se dimers lead to the low optical frequencies with strong anharmonicity. This means that the existence of the localized Se-Se dimers in ZnSe_2 plays an important role in the strong anharmonicity. Furthermore, the particular transverse acoustic phonon modes with a strong local change of the pyrite parameter can induce strong anharmonicity. The strong anharmonicities of different phonons can lead to the low lattice thermal conductivity in ZnSe_2 . By calculating the electronic properties of ZnSe_2 , we find that both VBM and CBM are dominated by the antibonding character of Zn-Se and Se-Se, and the valence and conduction bands both show complex energy isosurfaces, which can contribute to the promising electrical transport properties of p -type and n -type ZnSe_2 . Combining the low lattice thermal conductivities and promising electrical transport properties, both p -type and n -type ZnSe_2 show excellent thermoelectric properties at different pressures, especially at 0 GPa: The maximum ZT values of p -type and n -type ZnSe_2 can reach 2.21 and 1.87, respectively. Our work shows that ZnSe_2 is an excellent thermoelectric material at both p -type and n -type doping. This work can provide a guidance and inspiration for seeking new promising thermoelectric materials containing nonmetallic dimers.

ACKNOWLEDGMENTS

This work was supported by the National Natural Science Foundation of China, Grants No. 11774347 and

No. 11474283. This work was supported by the China Scholarship Council. The authors are very grateful for a meaningful discussion with Dr. Y. Javed.

- [1] H. J. Goldsmid, *Introduction to Thermoelectricity* (Springer, Berlin, 2016).
- [2] J. Yang, L. Xi, W. Qiu, L. Wu, X. Shi, L. Chen, J. Yang, W. Zhang, C. Uher, and D. J. Singh, *Npj Comput. Mater.* **2**, 15015 (2016).
- [3] G. Joshi, H. Lee, Y. Lan, X. Wang, G. Zhu, D. Wang, R. W. Gould, D. C. Cuff, M. Y. Tang, M. S. Dresselhaus, G. Chen, and Z. Ren, *Nano Lett.* **8**, 4670 (2008).
- [4] S. Bathula, M. Jayasimhadri, A. Dhar, M. Saravanan, D. K. Misra, N. Singh, A. K. Srivastava, and R. C. Budhani, *MRS Proc.* **1490**, 51 (2013).
- [5] K. Biswas, J. He, I. D. Blum, C. I. Wu, T. P. Hogan, D. N. Seidman, V. P. Dravid, and M. G. Kanatzidis, *Nature (London)* **489**, 414 (2012).
- [6] B. Paul, P. K. Rawat, and P. Banerji, *Appl. Phys. Lett.* **98**, 262101 (2011).
- [7] A. D. Lalonde, Y. Pei, and G. J. Snyder, *Energy Environ. Sci.* **4**, 2090 (2011).
- [8] S. Il Kim, K. H. Lee, H. A. Mun, H. S. Kim, S. W. Hwang, J. W. Roh, D. J. Yang, W. H. Shin, X. S. Li, Y. H. Lee, G. J. Snyder, and S. W. Kim, *Science* **348**, 109 (2015).
- [9] F. Wu, H. Song, J. Jia, and X. Hu, *Bull. Mater. Sci.* **37**, 1007 (2014).
- [10] G. S. Nolas, D. T. Morelli, and T. M. Tritt, *Annu. Rev. Mater. Sci.* **29**, 89 (1999).
- [11] X. Meng, Y. Liu, B. Cui, D. Qin, J. Cao, W. Liu, Z. Liu, W. Cai, and J. Sui, *J. Mater. Chem. A* **6**, 20128 (2018).
- [12] X. Shi, J. Yang, J. R. Salvador, M. Chi, J. Y. Cho, H. Wang, S. Bai, J. Yang, W. Zhang, and L. Chen, *J. Am. Chem. Soc.* **133**, 7837 (2011).
- [13] G. S. Nolas, J. L. Cohn, G. A. Slack, and S. B. Schujman, *Appl. Phys. Lett.* **73**, 178 (1998).
- [14] M. Christensen, S. Johnsen, and B. B. Iversen, *Dalton Trans.* **39**, 978 (2010).
- [15] H. Zhu, R. He, J. Mao, Q. Zhu, C. Li, J. Sun, W. Ren, Y. Wang, Z. Liu, Z. Tang, A. Sotnikov, Z. Wang, D. Broido, D. J. Singh, G. Chen, K. Nielsch, and Z. Ren, *Nat. Commun.* **9**, 2497 (2018).
- [16] W. G. Zeier, J. Schmitt, G. Hautier, U. Aydemir, Z. M. Gibbs, C. Felser, and G. J. Snyder, *Nat. Rev. Mater.* **1**, 16032 (2016).
- [17] H. Zhu, J. Mao, Y. Li, J. Sun, Y. Wang, Q. Zhu, G. Li, Q. Song, J. Zhou, Y. Fu, R. He, T. Tong, Z. Liu, W. Ren, L. You, Z. Wang, J. Luo, A. Sotnikov, J. Bao, K. Nielsch, G. Chen, D. J. Singh, and Z. Ren, *Nat. Commun.* **10**, 270 (2019).
- [18] C. Gayner and K. K. Kar, *Prog. Mater. Sci.* **83**, 330 (2016).
- [19] T. Jia, Z. Feng, S. Guo, X. Zhang, and Y. Zhang, *ACS Appl. Mater. Interfaces* **12**, 11852 (2020).
- [20] T. A. Bither, R. J. Bouchard, W. H. Cloud, P. C. Donohue, and W. J. Siemons, *Inorg. Chem.* **7**, 2208 (1968).
- [21] G. Kresse and J. Furthmüller, *Phys. Rev. B* **54**, 11169 (1996).
- [22] G. Kresse and D. Joubert, *Phys. Rev. B* **59**, 1758 (1999).
- [23] J. P. Perdew, K. Burke, and M. Ernzerhof, *Phys. Rev. Lett.* **77**, 3865 (1996).
- [24] H. J. Monkhorst and J. D. Pack, *Phys. Rev. B* **13**, 5188 (1976).
- [25] J. Heyd, G. E. Scuseria, and M. Ernzerhof, *J. Chem. Phys.* **118**, 8207 (2003).
- [26] A. V. Krukau, O. A. Vydrov, A. F. Izmaylov, and G. E. Scuseria, *J. Chem. Phys.* **125**, 224106 (2006).
- [27] A. Togo, F. Oba, and I. Tanaka, *Phys. Rev. B* **78**, 134106 (2008).
- [28] J. Carrete, B. Vermeersch, A. Katre, A. van Roekeghem, T. Wang, G. K. H. Madsen, and N. Mingo, *Comput. Phys. Commun.* **220**, 351 (2017).
- [29] W. Li, J. Carrete, N. A. Katcho, and N. Mingo, *Comput. Phys. Commun.* **185**, 1747 (2014).
- [30] G. K. H. Madsen, J. Carrete, and M. J. Verstraete, *Comput. Phys. Commun.* **231**, 140 (2018).
- [31] J. Bardeen and W. Shockley, *Phys. Rev.* **80**, 72 (1950).
- [32] H. Lee, *Thermoelectrics Design and Materials* (Wiley, Chichester, 2016).
- [33] Z. M. Gibbs, F. Ricci, G. Li, H. Zhu, K. Persson, G. Ceder, G. Hautier, A. Jain, and G. J. Snyder, *Npj Comput. Mater.* **3**, 8 (2017).
- [34] R. Guo, X. Wang, Y. Kuang, and B. Huang, *Phys. Rev. B* **92**, 115202 (2015).
- [35] Z. Feng, T. Jia, J. Zhang, Y. Wang, and Y. Zhang, *Phys. Rev. B* **96**, 235205 (2017).
- [36] F. Q. Wang, Y. Guo, Q. Wang, Y. Kawazoe, and P. Jena, *Chem. Mater.* **29**, 9300 (2017).
- [37] S. Guo, T. Jia, and Y. Zhang, *J. Phys. Chem. C* **123**, 18824 (2019).
- [38] Y. I. Ravich, B. A. Efimova, and V. I. Tamarchenko, *Phys. Status Solidi* **43**, 453 (1971).
- [39] A. Jain, S. P. Ong, G. Hautier, W. Chen, W. D. Richards, S. Dacek, S. Cholia, D. Gunter, D. Skinner, G. Ceder, and K. A. Persson, *APL Mater.* **1**, 011002 (2013).
- [40] See Supplemental Material at <http://link.aps.org/supplemental/10.1103/PhysRevB.102.125204> for the pressure-composition phase diagrams of $\text{Zn}_x\text{Se}_{1-x}$ at different pressures in detail; the contribution of the stretching of Se-Se bonds in the dimers to the high-frequency optical phonon modes in ZnSe_2 at 0 GPa; the phonon dispersions and the corresponding distribution of anharmonicities ($\gamma_{iq} = -\frac{V}{\omega_{iq}} \frac{\partial \omega_{iq}}{\partial V}$) in ZnSe_2 at 10 GPa; the symmetry degeneracies (D_s) and carrier effective masses ($m_{\alpha\beta}^*$) of different energy valleys at different bands along different directions (\vec{D}) in ZnSe_2 at 0 and 10 GPa; the calculated electronic relaxation times from the polar optical phonon scattering (τ_{po}) in ZnSe_2 at 0 GPa; the calculated electronic thermal conductivities (κ_e) in ZnSe_2 at 0 and 10 GPa (see, also, Refs. [32,33,70] therein).
- [41] A. Savin, R. Nesper, S. Wengert, and T. F. Fässler, *Angew. Chem. Int. Ed.* **36**, 1808 (1997).
- [42] D. A. Broido, M. Malorny, G. Birner, N. Mingo, and D. A. Stewart, *Appl. Phys. Lett.* **91**, 231922 (2007).
- [43] M. Arrigoni, J. Carrete, N. Mingo, and G. K. H. Madsen, *Phys. Rev. B* **98**, 115205 (2018).

- [44] A. Togo, L. Chaput, and I. Tanaka, *Phys. Rev. B* **91**, 094306 (2015).
- [45] B. Dongre, J. Carrete, N. Mingo, and G. K. H. Madsen, *MRS Commun.* **8**, 1119 (2018).
- [46] L.-D. Zhao, S.-H. Lo, Y. Zhang, H. Sun, G. Tan, C. Uher, C. Wolverton, V. P. Dravid, and M. G. Kanatzidis, *Nature (London)* **508**, 373 (2014).
- [47] G. A. Akhmedova and D. S. Abdinov, *Inorg. Mater.* **45**, 854 (2009).
- [48] P. B. Allen and J. L. Feldman, *Phys. Rev. B* **48**, 12581 (1993).
- [49] D. A. Broido, A. Ward, and N. Mingo, *Phys. Rev. B* **72**, 014308 (2005).
- [50] A. Fischer, E.-W. Scheidt, W. Scherer, D. E. Benson, Y. Wu, D. Eklöf, and U. Häussermann, *Phys. Rev. B* **91**, 224309 (2015).
- [51] Y. He, T. Day, T. Zhang, H. Liu, X. Shi, L. Chen, and G. J. Snyder, *Adv. Mater.* **26**, 3974 (2014).
- [52] Y. Zheng, C. Liu, L. Miao, C. Li, R. Huang, J. Gao, X. Wang, J. Chen, Y. Zhou, and E. Nishibori, *Nano Energy* **59**, 311 (2019).
- [53] Y. Zhang, E. Skoug, J. Cain, V. Ozoliņš, D. Morelli, and C. Wolverton, *Phys. Rev. B* **85**, 054306 (2012).
- [54] G. Qin, X. Zhang, S.-Y. Yue, Z. Qin, H. Wang, Y. Han, and M. Hu, *Phys. Rev. B* **94**, 165445 (2016).
- [55] S. A. Miller, P. Gorai, B. R. Ortiz, A. Goyal, D. Gao, S. A. Barnett, T. O. Mason, G. J. Snyder, Q. Lv, V. Stevanović, and E. S. Toberer, *Chem. Mater.* **29**, 2494 (2017).
- [56] D. T. Morelli, V. Jovicic, and J. P. Heremans, *Phys. Rev. Lett.* **101**, 035901 (2008).
- [57] T. Jia, G. Chen, and Y. Zhang, *Phys. Rev. B* **95**, 155206 (2017).
- [58] C. Chang and L.-D. Zhao, *Mater. Today Phys.* **4**, 50 (2018).
- [59] Y. Zhang, V. Ozoliņš, D. Morelli, and C. Wolverton, *Chem. Mater.* **26**, 3427 (2014).
- [60] Y. Zhang, S. Hao, L. D. Zhao, C. Wolverton, and Z. Zeng, *J. Mater. Chem. A* **4**, 12073 (2016).
- [61] W. Li and N. Mingo, *Phys. Rev. B* **91**, 144304 (2015).
- [62] E. D. Stevens, M. L. DeLucia, and P. Coppens, *Inorg. Chem.* **19**, 813 (1980).
- [63] L. D. Zhao, H. J. Wu, S. Q. Hao, C. I. Wu, X. Y. Zhou, K. Biswas, J. Q. He, T. P. Hogan, C. Uher, C. Wolverton, V. P. Dravid, and M. G. Kanatzidis, *Energy Environ. Sci.* **6**, 3346 (2013).
- [64] R. Dronskowski and P. E. Bloechl, *J. Phys. Chem.* **97**, 8617 (1993).
- [65] V. L. Deringer, A. L. Tchougréeff, and R. Dronskowski, *J. Phys. Chem. A* **115**, 5461 (2011).
- [66] S. Maintz, V. L. Deringer, A. L. Tchougréeff, and R. Dronskowski, *J. Comput. Chem.* **34**, 2557 (2013).
- [67] S. Maintz, V. L. Deringer, A. L. Tchougréeff, and R. Dronskowski, *J. Comput. Chem.* **37**, 1030 (2016).
- [68] A. Bhatia, G. Hautier, T. Nilgianskul, A. Miglio, J. Sun, H. J. Kim, K. H. Kim, S. Chen, G.-M. Rignanese, X. Gonze, and J. Suntivich, *Chem. Mater.* **28**, 30 (2016).
- [69] Brian K. Ridley, *Quantum Processes in Semiconductors* (Oxford University Press, New York, 2013).
- [70] H. B. Callen, *Phys. Rev.* **76**, 1394 (1949).